Structure and magnetism of mixed-valent iron oxysulfides $Sr_3Fe_4O_6S_2$ ($Sr_3(Fe^{3+})_2O_5(Fe^{2+})_2OS_2$) and $Sr_4Fe_4O_7S_2$ ($Sr_4(Fe^{3+})_2O_6(Fe^{2+})_2OS_2$)

Alexis N Gillette,[a] Annabel R Lyon,[a] Stanislav Savvin,[b,c] Ines Puente-Orench,[b] Sepideh Rahimisheikh,[d] Joke Hadermann,[d] Magali Gimeno,[a] Michael L. Neidig,[a] and Simon J Clarke* [a]

Supplementary Information

1. Synthetic Details

In the ceramic synthesis of $Sr_3Fe_2O_5Fe_2OS_2$ (compound **1**) and $Sr_4Fe_2O_6Fe_2OS_2$ (compound **2**), stoichiometric amounts of SrO, Fe_2O_3 (Alfa Aesar, 99.998%), Fe (Alfa Aesar, 99+%), and S (Sigma Aldrich, 99.98%) were combined in an agate mortar and pestle under an Ar atmosphere. SrO was obtained from the decomposition of $SrCO_3$ (Alfa Aesar, 99.994%) under dynamic vacuum and its identity and purity were then confirmed by in-house X-ray powder diffraction (XRPD) on a Bruker D8 Advance Eco instrument (Cu-$K\alpha$ radiation). The powder mixtures were then pressed into pellets of 13 mm diameter and placed into alumina crucibles which were subsequently sealed in evacuated silica tubes under dynamic vacuum while the bottom of the silica tube was dipped in liquid N_2 in a glass dewar to prevent the sublimation and loss of S. The sealed tubes were then heated at 1˚C per minute to 900˚C, and this temperature was maintained for a period of 48 hours before cooling to room temperature at the natural rate of the furnace. The products were all polycrystalline black powders stable to ambient moist air. Single crystal growth attempts have so far not been fruitful.

2. Structural Characterisation

X-ray Powder Diffraction.

Data for monitoring the course of reactions and assessing the purity of starting materials were collected on a Bruker D8 Advance ECO diffractometer using Cu-$K\alpha$ radiation and with an energy-discriminating detector used to minimise fluorescence from Fe.

Data for detailed structural analysis were obtained using the beamline I11 at the Diamond Light Source. Here Monochromatic X-rays of approximately 0.82 Å wavelength (determined accurately by refinement against a silicon standard at the start of each beam time session) were used to illuminate finely ground powder samples contained in 0.5 mm diameter borosilicate glass capillaries (or silica glass capillaries for high temperature measurements). Data were collected using the multi-angle Mythen Position-Sensitive Detector (PSD) and variable-temperature measurements down to 100 K were performed using an Oxford Cryosystems Cryostream plus. A hot-air blower was used to access temperatures up to 900 K.

Neutron powder Diffraction.

Variable temperature neutron powder diffraction (NPD) data were collected on the constant wavelength diffractometers D2B (Compounds **1** & **2**), D1B (Compound **1**) and XtremeD (Compound **2**) at the Institut Laue Langevin, Grenoble, France, and (at 300 K) on the time-of-flight instrument, GEM (ISIS facility, UK). On D1B, neutrons of wavelength 2.52 Å selected using pyrolytic graphite (002) monochromator were used along with a multi-angle detector to gather variable temperature data between 5K and ambient temperature to show the evolution of the low-angle magnetic scattering. On D2B, 1.59 Å neutrons selected using a Ge (335) monochromator were used to provide optimal nuclear data at the expense of lower resolution on the low-angle magnetic data. On XtremeD, neutrons of wavelength 2.44 Å were selected by a Si (115) monochromator. For all the NPD measurements the samples of about 3g in mass were containing in thin-walled vanadium cylinders.

Table S1a. Refined crystal structures for **1** and **2** from XRPD data collected on I11 (Diamond) using the PSD detector at ambient temperature.

	1 – $Sr_3Fe_2O_5Fe_2OS_2$				**2** – $Sr_4Fe_2O_6Fe_2OS_2$			
Sample ID	ANG047b				AL021			
Space group	*P*4/*mmm* (No.123)				*I*4/*mmm* (No. 139)			
a (Å)	3.9615(6)				3.945892(8)			
c (Å)	13.519(9)				31.9730(1)			
V (Å^3)	212.18(1)				497.822(3)			
atom	site	*x*	*y*	*z*	site	*x*	*y*	*z*
Sr1	1*a*	0	0	0	4*e*	0	0	0.29308(6)
Sr2	2*g*	0	0	0.27284(8)	4*e*	0	0	0.40291(7)
Fe1	2*h*	½	½	0.13841(9)	4*e*	½	½	0.34257(5)
Fe2	2*e*	½	0	½	4*c*	½	0	½
O1	4*i*	½	0	0.1593(2)	8*g*	½	0	0.35283(5)
O2	1*b*	0	0	½	2*b*	0	0	½
O3	1*c*	½	½	0	4*e*	½	½	0.28339(8)
S	2*h*	½	½	0.3727(1)	4*e*	½	½	0.44660(2)

Table S1b. Refined crystal structures for **1** and **2** from NPD data collected on D2B (ILL) and GEM (ISIS), respectively, at ambient temperature.

	1 – $Sr_3Fe_2O_5Fe_2OS_2$				**2** – $Sr_4Fe_2O_6Fe_2OS_2$			
Sample ID	ANG022				AL010			
Space group	*P*4/*mmm* (No.123)				*I*4/*mmm* (No. 139)			
a (Å)	3.95508(8)				3.9388(6)			
c (Å)	13.5256(5)				31.923(5)			
V (Å^3)	211.58(1)				495.3(2)			
atom	site	*x*	*y*	*z*	site	*x*	*y*	*z*
Sr1	1*a*	0	0	0	4*e*	0	0	0.29294(3)
Sr2	2*g*	0	0	0.2741(3)	4*e*	0	0	0.40294(3)
Fe1	2*h*	½	½	0.1384(2)	4*e*	½	½	0.34242(3)
Fe2	2*e*	½	0	½	4*c*	½	0	½
O1	4*i*	½	0	0.1556(2)	8*g*	½	0	0.35277(2)
O2	1*b*	0	0	½	2*b*	0	0	½
O3	1*c*	½	½	0	4*e*	½	½	0.28342(4)
S	2*h*	½	½	0.3806(8)	4*e*	½	½	0.44620(7)

Table S2. Selected refined bond lengths from XRPD and NPD patterns collected at 300 K using the PSD detector on I11 and on D2B respectively (For D2B refinements see Fig. S2 and GEM refinements for **2** in Fig. S13). Bond valence calculations were performed using literature data from Brown and Altermatt[1] along with refined bond lengths values from this table. (Note: Fe2-O2 = *a* / 2 hence the small esds).

	1 – $Sr_3Fe_2O_5Fe_2OS_2$ (*P*4/*mmm* No. 123)		**2** – $Sr_4Fe_2O_6Fe_2OS_2$ (*I*4/*mmm* No. 139)		
Sample ID	ANG022	ANG022	AL021	AL021	AL010
Instrument	I11 PSD	D2B	I11 PSD	D2B	GEM
R_{wp} (%)	6.069	6.828	4.473	4.945	4.252
a (Å)	3.95867(4)	3.95508(8)	3.94589(1)	3.94798(5)	3.9387(6)
c (Å)	13.5357(3)	13.5256(5)	31.9730(1)	31.9950(5)	31.921(5)
V (Å^3)	212.120(7)	211.58(1)	497.822(3)	498.69(1)	495.2(2)
Fe1-O1 (Å)	1.999(1)	1.9912(5)	2.0029(5)	2.0011(4)	1.9969(2)
Fe1-O3 (Å)	1.875(5)	1.872(3)	1.904(4)	1.893(3)	1.884(2)
Fe2-O2 (Å)	1.97933(3)	1.97754(5)	1.97295(1)	1.97399(3)	1.9694(3)
Fe2-S (Å)	2.596(4)	2.553(7)	2.610(1)	2.611(3)	2.613(2)
Fe1 BVS	2.876	2.921	2.745	2.775	2.816
Fe2 BVS	2.134	2.276	2.127	2.121	2.128

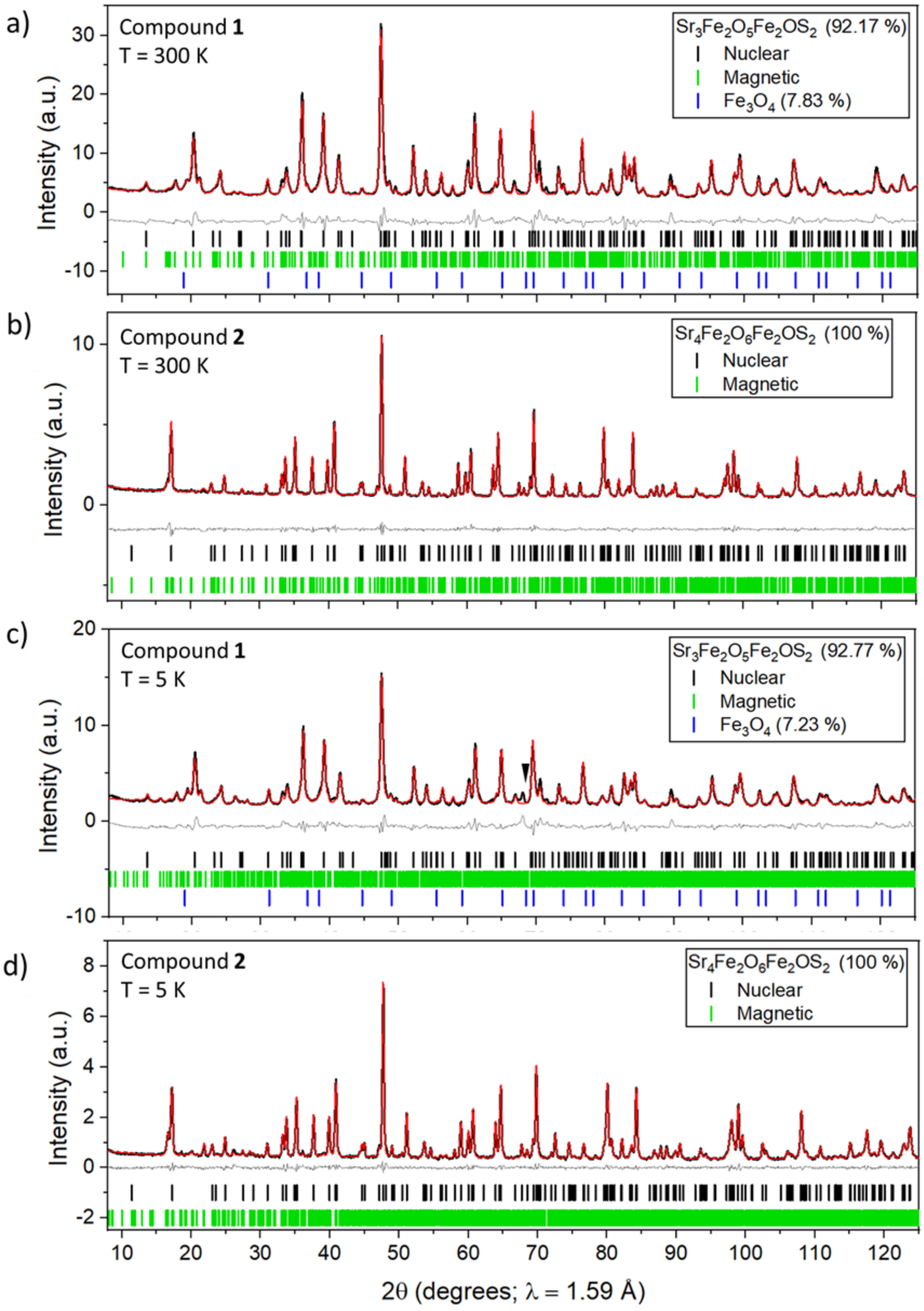

Figure S1. Rietveld refinement plots for a) **1** (ANG022) and b) **2** (AL021) at 300 K as well as c) **1** and d) **2** at 5 K collected on D2B showing the observed (black), calculated (red) and difference (grey) curves. The sample of **1** contains slightly more Fe_3O_4 than the sample measured on D1B to probe the magnetic ordering (main text), and an additional reflection at low temperatures (arrowed) of uncertain origin.

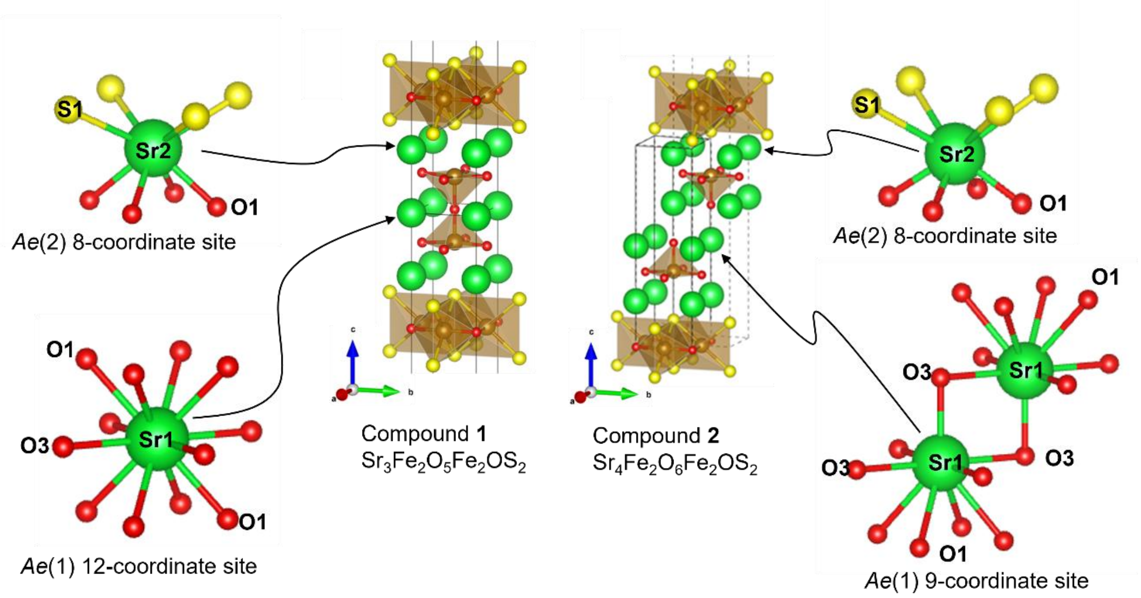

	1: $Sr_3Fe_2O_5Fe_2OS_2$ *P*4/*mmm* (No. 123)		**2:** $Sr_4Fe_2O_6Fe_2OS_2$ *I*4/*mmm* (No. 139)	
Bond	Bond length (Å)	Number of bonds	Bond length (Å)	Number of bonds
Sr(1)-O(1)	2.847(3)	[8]	2.748(2)	[4]
Sr(1)-O(3)	2.791(4)	[4]	2.8088(4)	[4]
			2.447(3)	[1]
Sr(2)-O(1)	2.573(4)	[4]	2.542(2)	[4]
Sr(2)-S(1)	3.103(4)	[4]	3.122(3)	[4]

Figure S2. Strontium coordination sites and table of interatomic distances from room temperature neutron powder diffraction data for compounds **1** & **2** (D2B) (Table S1b, Fig. S1).

Sample variation in Compound 1 ($Sr_3Fe_2O_5Fe_2OS_2$)

In compound **1** ($Sr_3Fe_2O_5Fe_2OS_2$), we discovered variation in the XRPD patterns observed from sample to sample. As shown in Fig. S3(a), some samples contain broad diffuse peaks that cannot be assigned to obvious impurities and which shift in position along with the sharp Bragg peaks, which suggest that they may be arising due to the sample itself. A full investigation of this phenomenon, and how it may relate to the complex microstructure revealed in Figure 7 of the main text, and in the additional electron microscopy results shown in Figure S5 is in progress. Furthermore, in some samples of compound **1** there are peaks that split (most obviously the (200) and (020) peaks shown in Fig. S3(b)) which suggest an orthorhombic (or lower symmetry) distortion. How and why this distortion occurs is still under investigation.

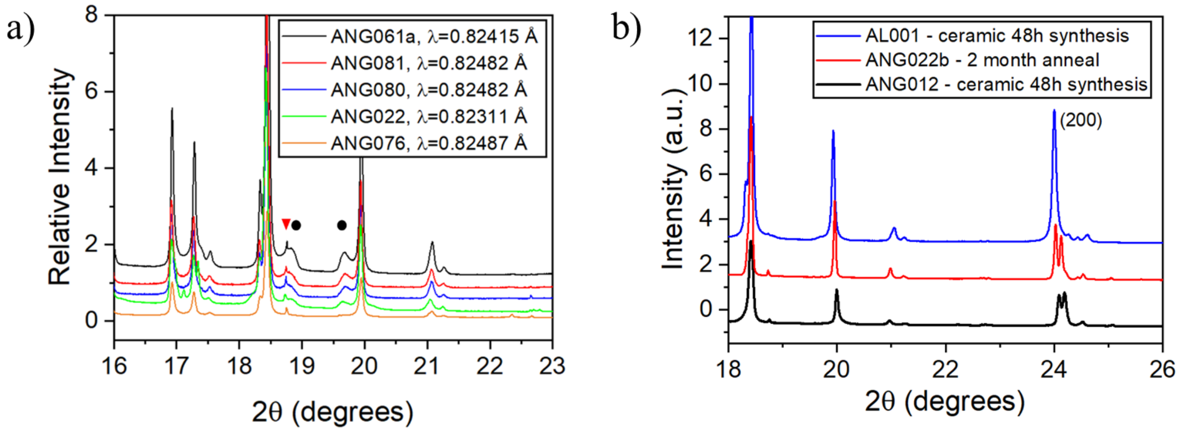

Figure S3. **(a)** XRPD patterns measured on I11 for varying samples of **1** that display diffuse peaks (black circles); Red triangle indicates Fe_3O_4 (311) reflection) as well as **(b)** a splitting of the (200) and (020) peaks in some samples indicating an orthorhombic distortion (λ = 0.82 Å).

In the case of the orthorhombic samples of **1**, there is a high-temperature orthorhombic to tetragonal phase transition at 500 K (Fig S4).

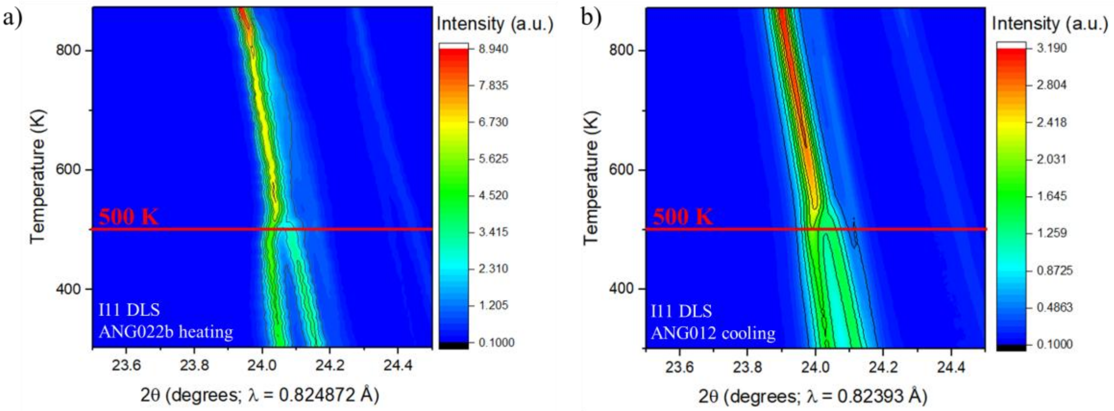

Figure S4. Portions of contour plots of variable temperature XRPD data from two samples of Compound **1** that show a splitting of the (200) and (020) peaks (suggesting of a reduction to orthorhombic or lower symmetry) at ambient temperatures. Above 500 K the tetragonal structure evident in other samples at room temperature transition is found. In (a) data are presented on heating. In (b), data on a different sample are presented on cooling. Both sets of data were collected on the I11 beamline at the Diamond light source using the Mythen PSD detector, with samples contained in sealed silica capillaries and with heating provided by a hot air blower.

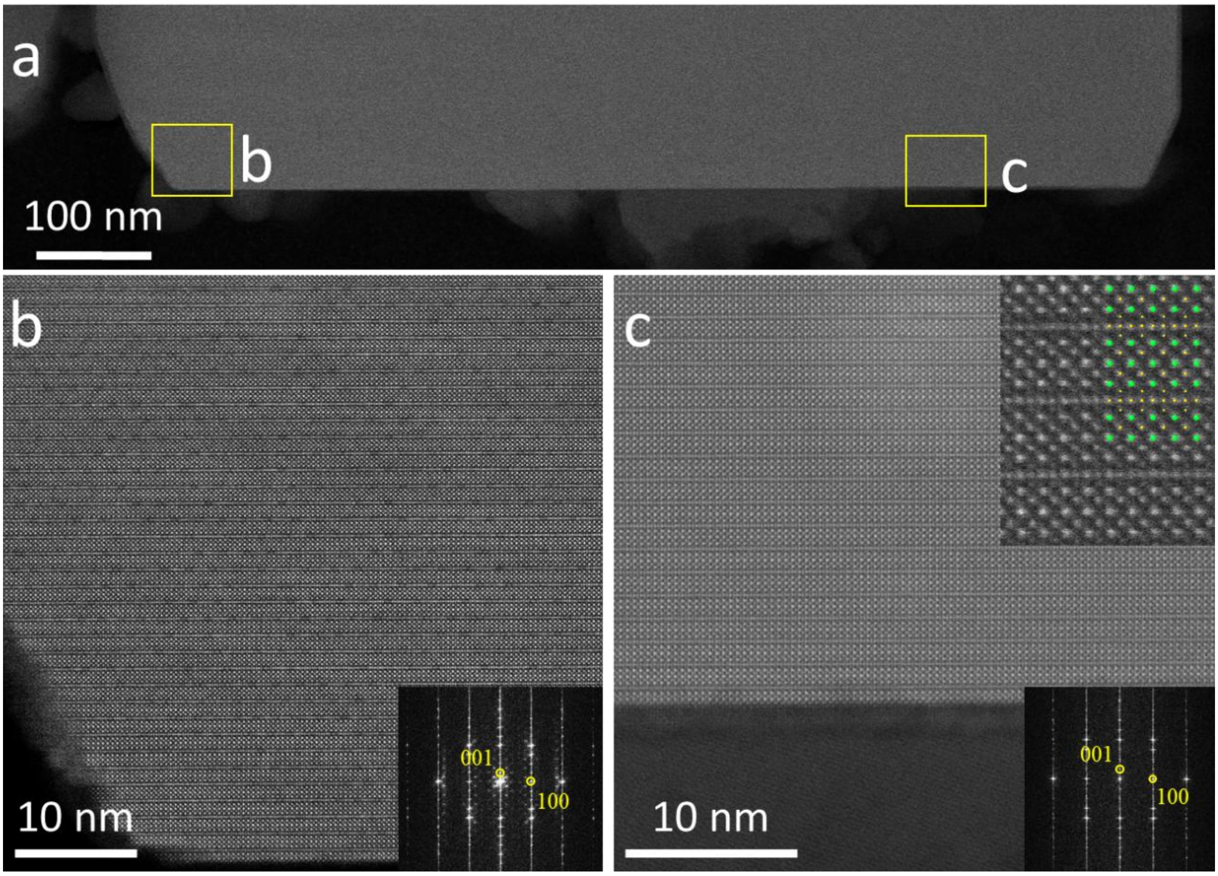

Figure S5. HAADF-STEM images at room temperature of a sample of compound **1** $Sr_3Fe_2O_5Fe_2OS_2$ (ANG022b obtained from a lengthy annealing of a tetragonal as-made sample ANG022 – see also Figure S3(b) and S4(a)) that had orthorhombic or lower symmetry according to high-resolution XRPD data. For this TEM experiment, we cleaned the FIB lamella with a plasma cleaner to prevent contamination growth triggered by the electron beam. For this, the assembled lamella was treated on the TEM holder with an Ar plasma in a vacuum chamber for 90 seconds. Then, the sample was directly transferred to the microscope without any further modification. (a) shows the high magnification HAADF-STEM images from the edge of the FIB sample oriented to the [010] zone-axis. In (b) there is a clear modulation visible in the contrast, which could indicate the presence of ordered vacancies; the fast-Fourier transform (FFT) (inset to (b)) shows satellite peaks around the main reflections corresponding with the periodicity of the features in the HAADF-STEM image. However, as shown in (c) other regions of the same sample do not show such features. This underlines the complexity of these compounds as indicated also by Fig. 7 (for a tetragonal sample) in the main article.

Variable Temperature powder diffraction and microstructure of compound 2 ($Sr_4Fe_2O_6Fe_2OS_2$).

In compound **2** ($Sr_4Fe_2O_6Fe_2OS_2$), there was no sign of measurable sample variation or anomalies in the powder diffraction patterns, nor did HAADF-STEM imaging show any evidence for the complex structural features evident in Compound **1.** The image in Fig. S7, which is representative, shows structural order on a long length scale. In compound **2** variable temperature XRPD revealed an obvious structural transition (Fig. S6) between 400 and 450 K which is likely a magnetoelastic coupling between the structure and the ordering of the Fe^{3+} (Fe1) magnetic moments. The slight kink at 300 K appears to be an instrumental anomaly associated with a change in temperature control mechanism at around room temperature.

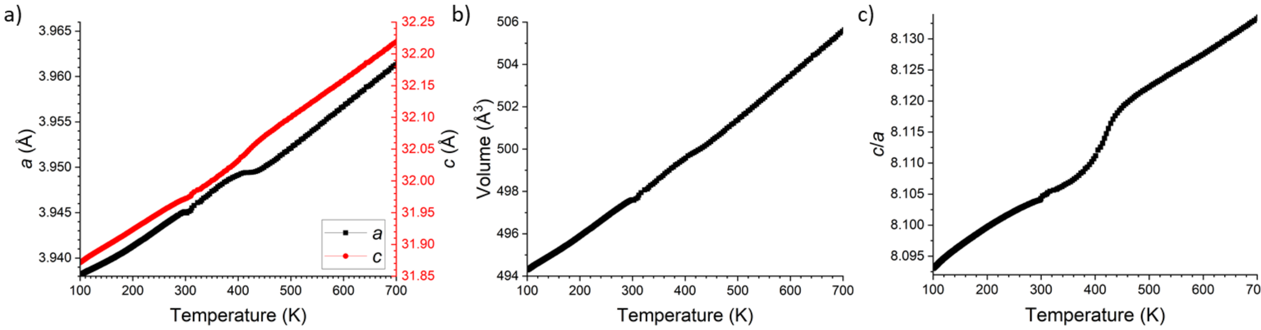

Figure S6. Variable temperature plot of refined a) lattice parameters, b) unit cell volume and c) the ratio between *c* and *a* lattice parameter for $Sr_4Fe_2O_6Fe_2OS_2$ (compound **2**) from SXRPD data collected on I11, DLS.

Microstructure of compound 2.

In contrast to the occurrence of large numbers of defects found in compound **1** (see main text and above), compound **2** was observed to have a microstructure with no such defects observed in the sample studied.

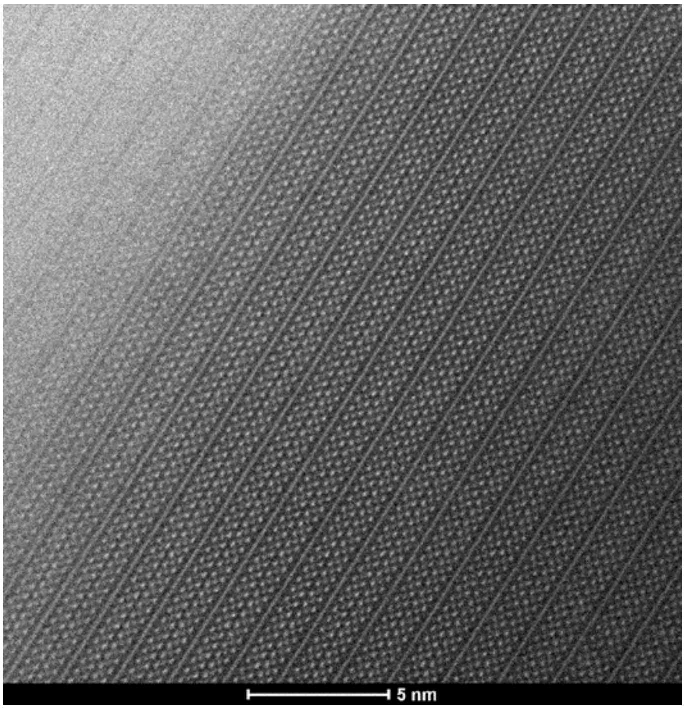

Figure S7. TEM image of a sample of a sample of compound **2** ($Sr_4Fe_2O_6Fe_2OS_2$) (sample AL010) showing no sign of the defects evident in compound **1** ($Sr_3Fe_2O_5Fe_2OS_2$) (Fig.7 and Fig. S5).

Magnetometry Data

The magnetic susceptibility data obtained for **1** (Fig. S8) using SQUID magnetometry reveals relatively little about the compounds magnetic behaviour as the measurement is dominated by the ferrimagnetism and the low temperature Verwey transition at 120 K of the Fe_3O_4 impurity which seems to be an intrinsic feature of this compound, and is presumably associated with the occurrence of defects observed in the electron microscopy measurements. The Verwey transition occurs around the temperature where the Fe2 layer orders antiferromagnetically according to NPD, so this transition is not observed in the magnetic susceptibility. The displacement from the origin of the magnetisation isotherm of **1** is suggesting of a glassy component to the magnetism, which may be associated with the occurrence of defects.

The magnetic susceptibility data obtained for **2** (Fig. S9) shows a transition starting from 410 K which we assign to the long-range ordering of Fe^{3+} ions within the Fe1 layer, consistent with the significant, but unsaturated, long range ordered moment of 2.14(2) μ_B per Fe(1) site found from NPD data at 300 K. This transition is coupled to a structural transition (Fig. S6). A broad feature in the magnetometry data between 100 and 150 K may be associated with the onset of magnetic ordering on the Fe(2) sublattice of **2**, which neutron diffraction data shows to be above 150 K (Fig. S13). A lower temperature transition at 100 K suggests a weak ferromagnetic component which may indicate a slight canting in the antiferromagnetic state. Like in **1** there is a slight displacement of the 5K magnetisation away from the origin, suggestive of glassiness which may be the origin of the divergence of the field cooled (FC) and zero-field cooled (ZFC) data above 100 K.

Further useful insight from magnetometry on these samples will likely require measurements on oriented single crystal samples.

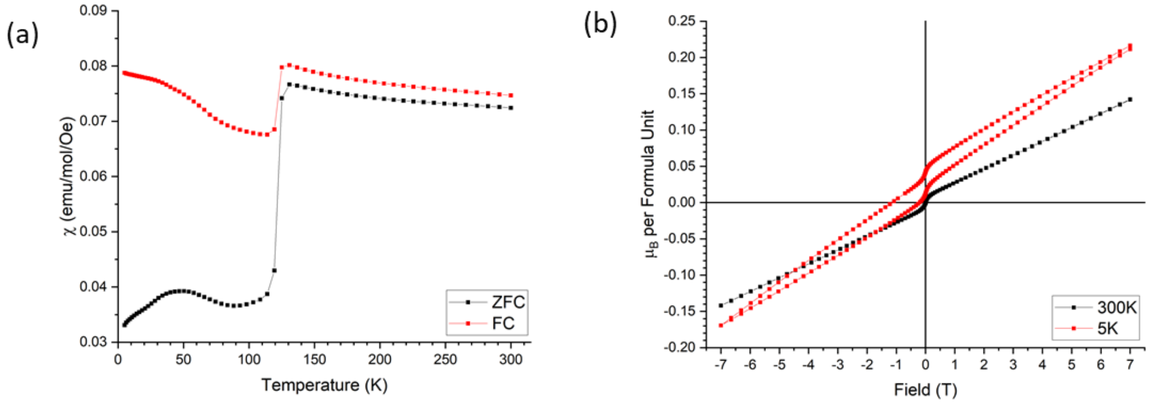

Figure S8. Magnetic susceptibility measurements for compound **1** ($Sr_3Fe_2O_5Fe_2OS_2$) (a) zero-field-cooled and field-cooled susceptibility with an applied field of 100 Oe between 5 – 300 K showing a transition due to a small contamination of Fe_3O_4. (b) the magnetization isotherms at 300 K and 5 K. The displacement of the 5K isotherm is indicative of a glassy component to the magnetism, likely associated with defects (see Figs 7 and S5).

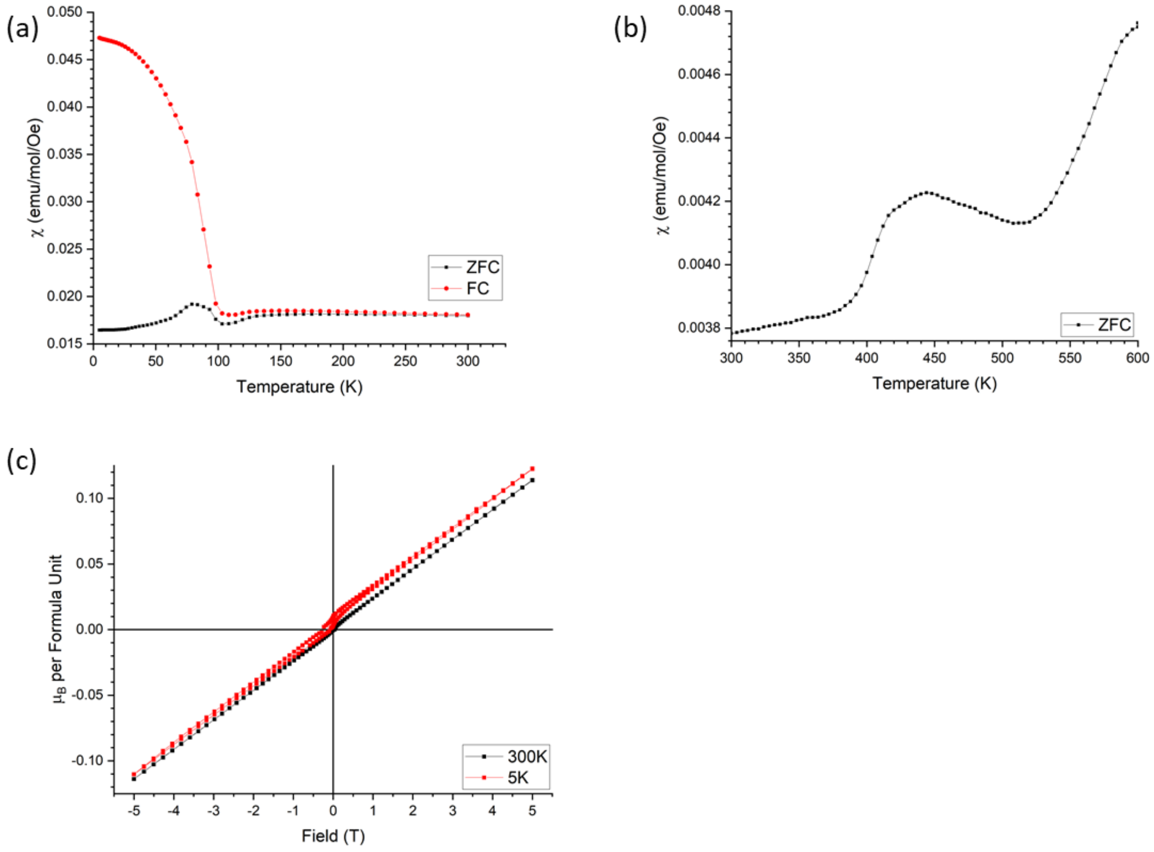

Figure S9. Magnetic susceptibility measurements for compound **2** ($Sr_4Fe_2O_6Fe_2OS_2$) zero-field-cooled and field-cooled susceptibility with an applied field of 100 Oe between 5 – 300 K showing a transition below 100 K, consistent with a small ferromagnetic component of uncertain origin. (b) High-temperature susceptibility (zero-field-cooled, 100 Oe) showing a broad transition coincident with the magnetic ordering and the structural transition shown in Fig. S6. Note that (a) and (b) were measured with different sample preparations and environments so do not coincide at 300 K. (c) Magnetization isotherms at 300 K and 5 K.

Magnetic Structure models for Compound 1 ($Sr_3Fe_2O_5Fe_2OS_2$):

As discussed in the main text, the neutron powder diffraction measurement does not enable a unique magnetic structure to be used to describe the magnetic structure of the Fe1 (Fe^{3+}) moments in **1**. The structure presented in the main text uses a single-phase model to model the scattering in which neighbouring double layers of antiferromagnetically ordered Fe1 moments are rotated relative to one another in the basal (*ab*) plane. All moments have the same magnitude. An indistinguishable model, again with all Fe1 moments equal, is to use two different co-existing magnetic structures. In these structures, illustrated in Fig. S10 the Fe1 double layer is still antiferromagnetically ordered via all the Fe-O-Fe connections involving the shared vertices of adjacent FeO_5 square pyramids. The difference between the two structures is that in structure **1A**, all the Fe1 double layers are in phase along the *c* direction and the magnetic unit cell and the structural cell have the same repeat along the stacking direction. In structure **1B**, alternate Fe1 layers are out of phase with one another as illustrated in Fig. S10. The two structures have different propagation vectors and give rise to two different sets of magnetic Bragg peaks. A simple linear combination of these two structures, to produce a single-phase model, results in unequal Fe moments. The alternative to this is the model described in the main text with a relative rotation of the moment directions in adjacent blocks. These various descriptions are indistinguishable by neutron powder diffraction (Fig. S11), with the relative intensities of the magnetic peaks being controlled by the rotation angle in the model presented in the main text, or by the ratio of structures **1A** to **1B**. Single crystal neutron diffraction measurements would be required to investigate this further.

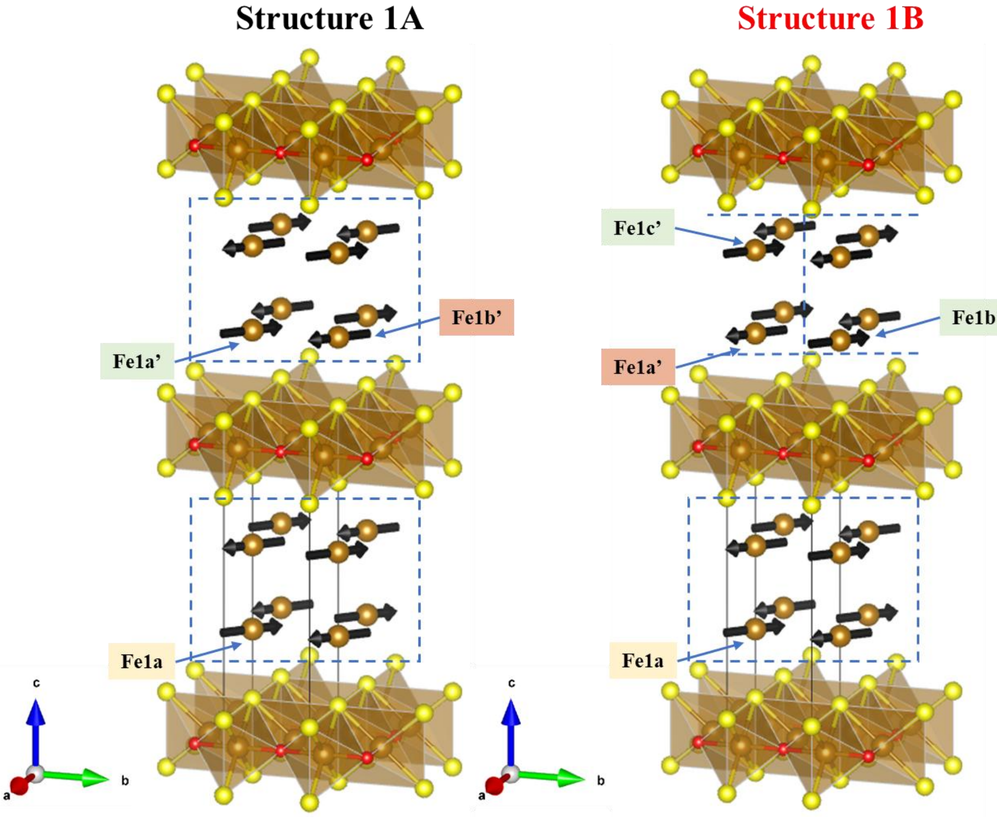

Figure S10. Magnetic structures **1A** and **1B**. A linear combination of these can be used to describe the magnetic scattering arising from Fe1 moments of identical magnitude as an alternative to the single-phase model presented in the main text.

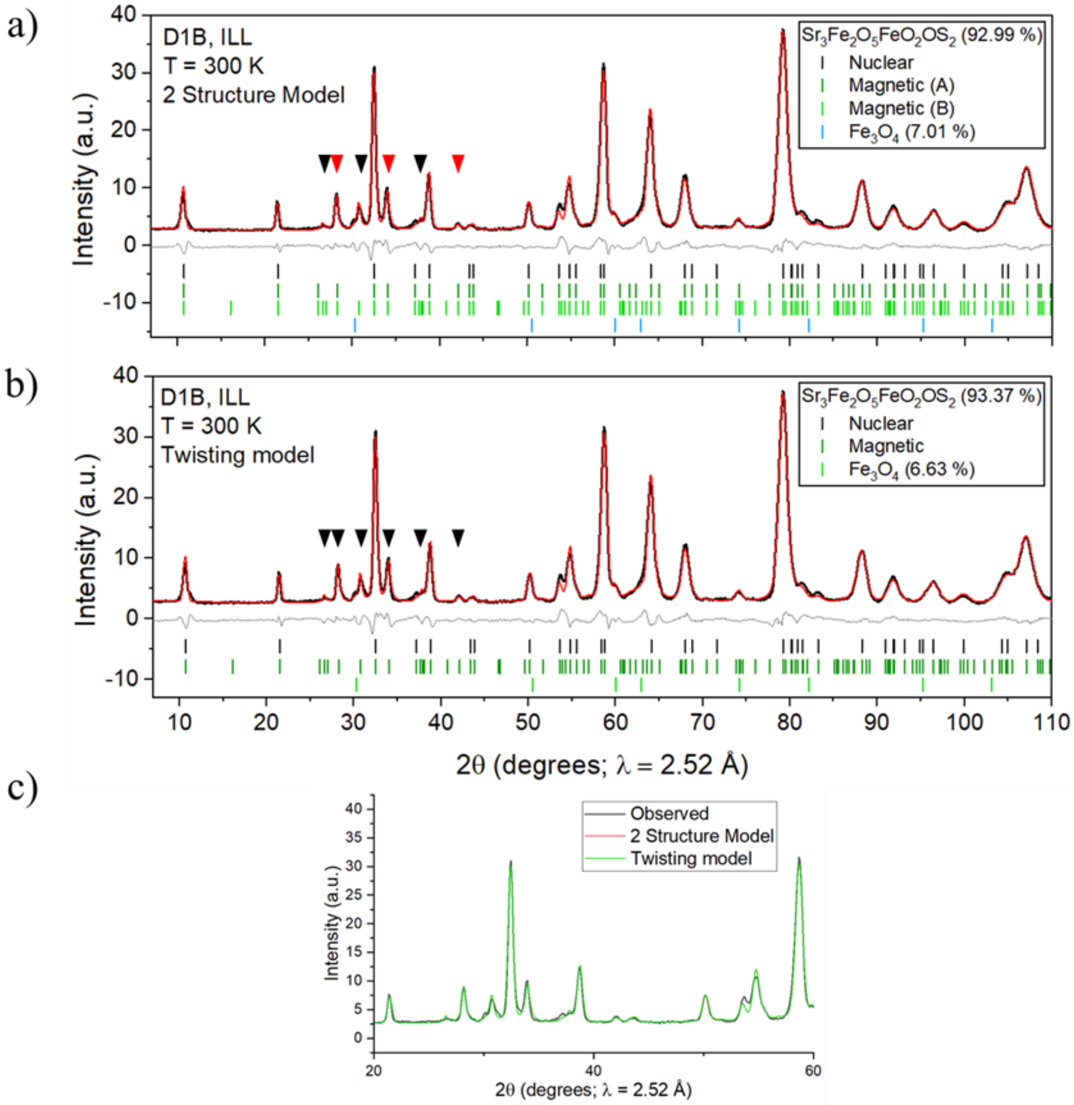

Figure S11. Rietveld refinements of the room temperature neutron powder diffraction pattern of $Sr_3Fe_2O_5Fe_2OS_2$ (**1**) collected on D1B. Observed (black), calculated (red) and difference (grey) curves are shown. In (a) structures **1A** and **1B** (see Fig S10) are used and their ratio refined. In this case black triangles correspond to peaks fit by structure **1A** and red peaks correspond to peaks fit by structure **1B**. In (b) the alternative model described in the main text is used in which there is a single magnetic phase and the moments “twist” through some angle from one double layer of Fe1 moments to the next. Refinement of the “twist” angle in (b) is equivalent to refining the ratio of structures **1A** and **1B** in (a). In both cases there is a single Fe moment amplitude. The calculated patterns overlap exactly (c) and cannot, in principle, be distinguished in a powder diffraction experiment.

Magnetic Structure of compound 2 ($Sr_4Fe_2O_6Fe_2OS_2$):

Just like in compound **1**, the magnetic moments of Fe^{2+} and Fe^{3+} within compound **2** order at different temperatures on different magnetic unit cells. At room temperature the Fe^{3+} ions are antiferromagnetically ordered in the *ab* plane and require a $\sqrt{2}a_{\mathrm{nuc}}$ by $\sqrt{2}a_{\mathrm{nuc}}$ by c_{nuc} expansion of the nuclear unit cell to be indexed. Tilting the Fe^{3+} moment out of the *ab* plane improves the goodness of fit in the refinement model, this is also observed for $Sr_4Fe_2O_6Cu_2S_2$ which contains the same Fe^{3+} layer. No exchange field operates in the c direction, thus, the Fe1-O1-Fe1 super exchange interaction dictates the room temperature magnetism of compound **2**. Consequently, as long as the antiferromagnetic relationship within FeO_5 sheets is maintained in the *ab* plane, magnetic moments in parallel FeO_5 sheets can be directed in any orientation with respect to one another. For the images in this paper all Fe^{3+} moments have been arbitrarily chosen to lie in the *bc* plane. On cooling below room temperature, Fe^{2+} ions order as described in the main text. The growth of these magnetic Bragg peaks can be seen in Fig. S13. This data was collected on XtremeD during sample cooling and so the temperature recorded may not be fully representative of the true sample environment over the duration of the scan. Using these results as a rough guide and extrapolating the data indicates the ordering of the Fe^{2+} layer at around 150 K. As referenced in the text, the magnetic model for compound **2** does not completely fit the observed diffraction patterns (red triangle in Fig. 5). We suspect the origin of this lies in the presence of magnetic stacking faults which arise due to the body centred unit cell of compound **2**.[2] Due to the primitive unit cell of compound **1** the same effect is not observed within this compound. In both compound **1** and compound **2** the Fe^{3+} and Fe^{2+} ions do not interact as they order on different magnetic sublattices with different periodicities and thus have different propagation vectors which should not interact.[3]

Table S3. Refined powder neutron refinement data for compound **2** ($Sr_4Fe_2O_6Fe_2OS_2$) at 300 K and 5 K.

Temperature (K)	300			5	
Sample ID	AL010	AL021	AL021	AL021	AL021
Instrument	GEM	XtremeD	D2B	XtremeD	D2B
R_{wp} (%)	4.252	3.610	4.945	4.087	5.566
a (Å)	3.939(6)	3.9358(2)	3.94798(5)	3.9351(2)	3.94006(6)
c (Å)	31.923(5)	31.901(3)	31.9950(5)	31.839(3)	31.8776(6)
V (Å^3)	495.3(2)	494.17(6)	498.69(1)	493.03(7)	494.87(2)
Saturated magnetic Fe^{3+}	2.3(1)	2.1(2)	3.1(4)	3.8(2)	3.7(2)
moment, μ_B Fe^{2+}	-	-	-	2.2(2)	1.8(2)
Angle of Fe^{3+} moment (°) (canted away from *c* axis)	47(1)	55(1)	60(1)	56(1)	56(1)

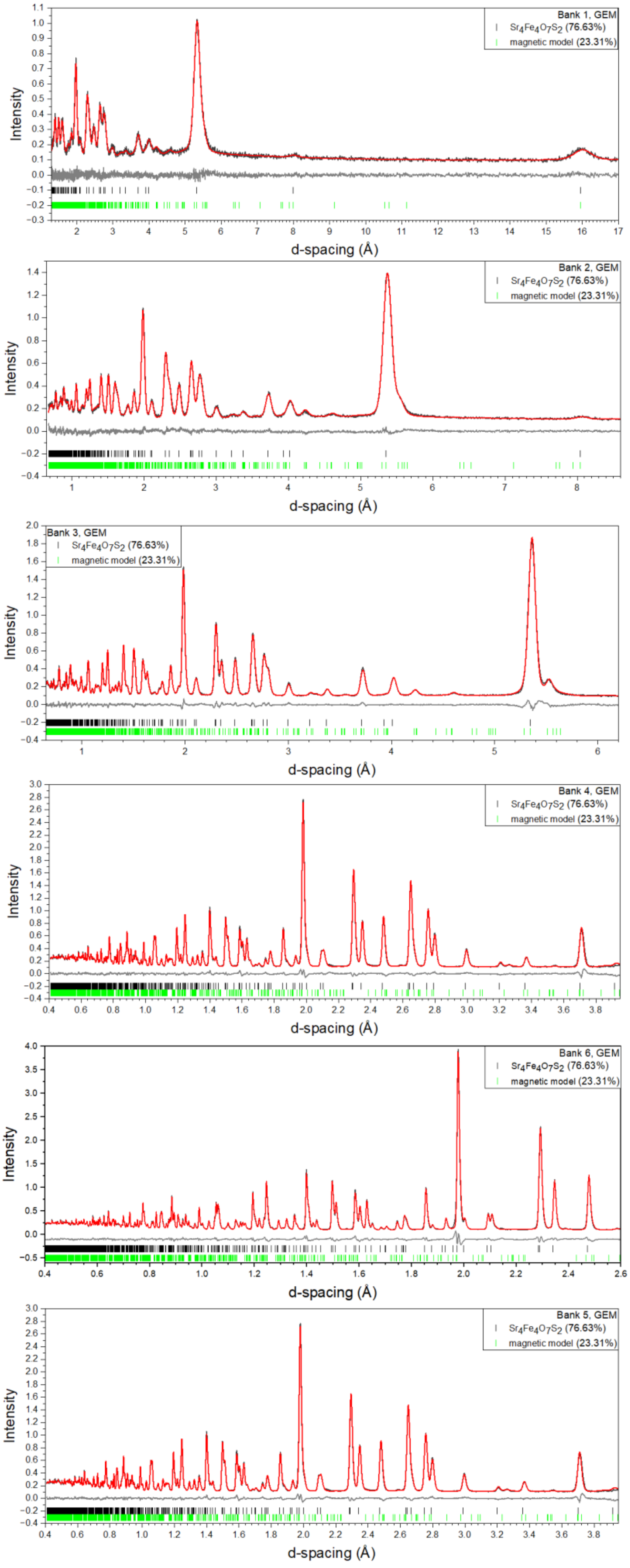

Figure S12. Rietveld refinements of the room temperature neutron powder diffraction pattern of $Sr_4Fe_2O_6Fe_2OS_2$ (**2**) (AL010) collected on GEM[5] banks 1-6. Observed (black), calculated (red) and difference (grey) curves are shown. See Tables S1b and S2.

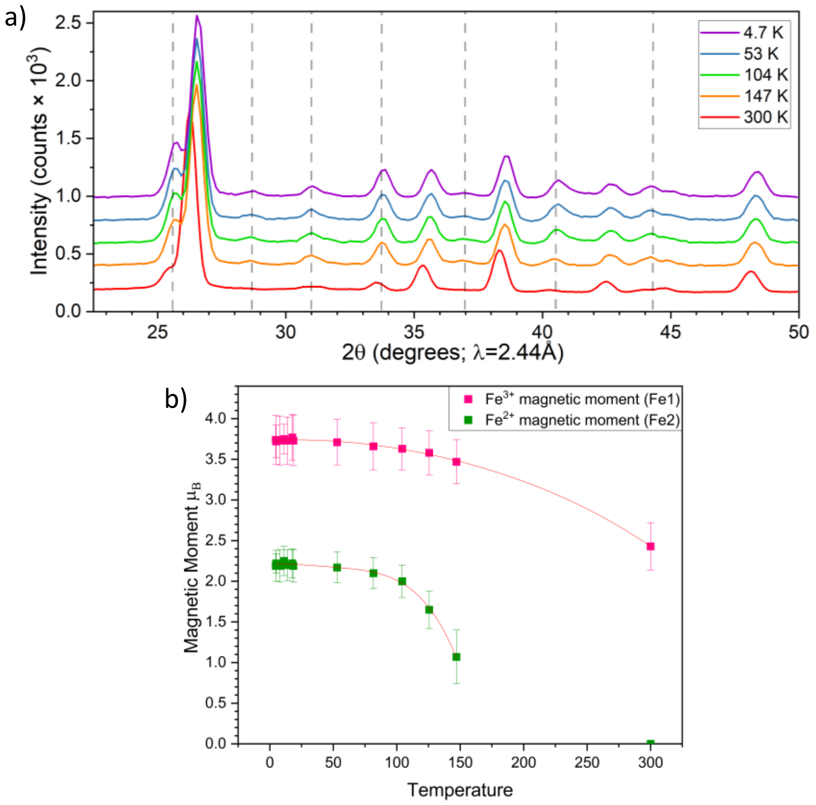

Figure S13. (a) Neutron diffraction patterns of **compound 2** measured on XtremeD during cooling from 300 K to 5 K. The growth of diffraction peaks (indicated by the grey dashed lines) result from the ordering of Fe^{2+} magnetic moments. (b) The refined magnetic moment of Fe^{2+} (green) and Fe^{3+} (pink) plotted against temperature. It should be noted that as measurements were recorded on cooling the temperature varied by up to ~ 10K for the duration of the measurement of each diffractogram in the region between 50 and 150 K.

Mössbauer Spectroscopy

^{57}Fe Mössbauer measurements were performed on non-enriched powder samples (contained in Delrin Mössbauer sample cups) using a See Co. MS4 Mössbauer spectrometer integrated with a Janis SVT-400T He/N2 cryostat for measurements at 80 K. Isomer shifts were determined relative to α-iron at 298 K. Spectra were fit using the program WMoss (See Co).

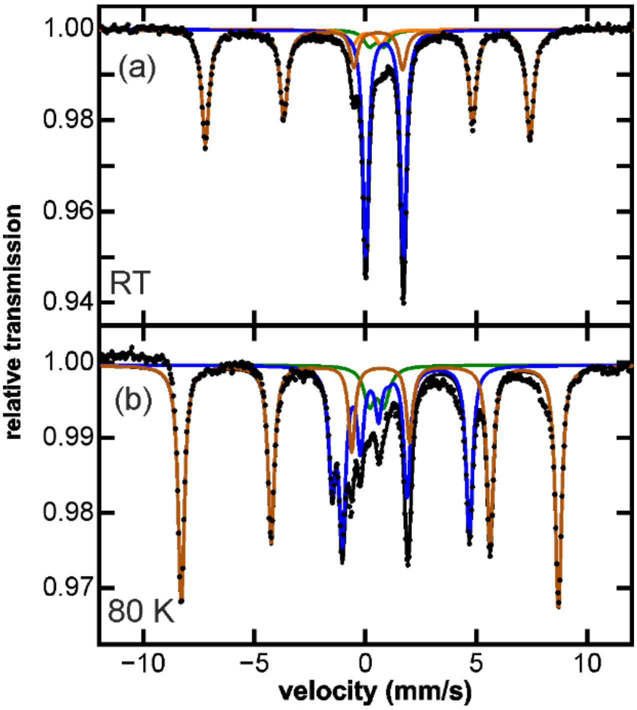

Figure S14. Reproduction of Fig. 6 from the main article showing the fits to Mössbauer spectra obtained at room temperature (~ 295 K) and 80 K. Table of fitted parameters appears below.

Table S4. Fit parameters for the ^{57}Fe Mössbauer spectra of compound **1** ($Sr_3Fe_2O_5Fe_2OS_2$) at room temperature (~ 295 K) and 80 K (Fig 6 and reproduced above as Fig SX for reference). δ is the isomer shift, ΔE_Q is the electric quadrupole splitting and H_{int} is the ordering field for the magnetically ordered species. For all Mössbauer spectra, uncertainties of the fit analyses were the following: δ ± 0.02 mm s^{-1}, ΔE_Q ± 2%, H_{int} ± 0.5% and percentage of total iron is ± 3 %. Note that the changes in the isomer shift from 300 K to 80 K have been previously observed for other relevant compounds[4] [Ref 19 in main article]].

Temp.	Component	δ (mm/s)	ΔE_Q (mm/s)	H_{int} (kG)	Population (%)	Signal origin
RT	Brown sextet	0.34	1.21	452.1	53	Fe1
	Blue doublet	0.87	1.70		38	Fe2
	Orange doublet	0.07	1.28		4	unknown
	Green doublet	0.51	0.65		5	unknown
80 K	Brown sextet	0.45	1.10	526.7	54	Fe1
	Blue sextet	1.01	1.70	177.1	40	Fe2
	Green doublet	0.51	0.65		6	unknown

---

[1] I.D. Brown, D. Altermatt, Bond-valence parameters obtained from a systematic analysis of the Inorganic Crystal Structure Database, *Acta Crystallogr. Sect. B.* 1985, **41**, 244–247, https://doi.org/10.1107/S0108768185002063.

[2] R. K. Oogarah, E. Suard, E. E. McCabe. Magnetic order and phase transition in the iron oxysulfide $La_2O_2Fe_2OS_2$. *J. Magn. Magn. Mater.*, 2018, **446**, 101–107.

[3] X. Xu, M. A. Jones, S. J. Cassidy, P. Manuel, F. Orlandi, M. Batuk, J. Hadermann, S. J. Clarke* Magnetic Ordering in the Layered Cr(II) Oxide Arsenides $Sr_2CrO_2Cr_2As_2$ and $Ba_2CrO_2Cr_2As_2$. *Inorg. Chem.* 2020, **59**, 15898–15912. https://doi.org/10.1021/acs.inorgchem.0c02415

[4] Y. Fuwa, M. Wakeshima, Y. Hinatsu, Crystal structure, magnetic properties, and Mössbauer spectroscopy of new layered iron oxyselenide $Nd_2Fe_2O_3Se_2$, *J. Phys.: Condens. Matter,* 2010, **22**, 346003. https://doi.org/10.1088/0953-8984/22/34/346003.

[5] W. G. Williams, R. M. Ibberson, P. Day, J. E. Enderby, GEM — General Materials Diffractometer at ISIS. *Physica B Condens Matter* 1997, **241–243**, 234–236. https://doi.org/10.1016/S0921-4526(97)00561-9.